Elucidating the structural properties of gold selenide nanostructures

Lerato F.E. Machogo[1], Musa Mthimunye[1], Rudo K. Sithole[1], Phumlani Tetyana[1,2], Neo Phao[1], Grace N. Ngubeni[1], Mbuso Mlambo[3], Phumlane S. Mduli[4], Poslet M. Shumbula[2] and Nosipho Moloto[1*]

[1]*Molecular Sciences Institute, School of Chemistry, University of the Witwatersrand, Private Bag 3, Wits, 2050, South Africa*
[2]*Advanced Materials Division, DST/Mintek Innovation Centre, Mintek, 200 Malibongwe Drive, Randburg, South Africa*
[3]*Department of Physics, University of Pretoria, Pretoria, 0002, South Africa*
[4]*Department of Chemistry, Durban University of Technology, P O Box 1334, Durban, 4000, South Africa*

*Corresponding Author: N. Moloto
Email: Nosipho.Moloto@wits.ac.za
Tel: +2711 717 6774
Fax: +2711 717 6749

Abstract

Noble transition metal chalcogenide gold selenide is a relatively unexplored layered material. Herein, we report on the synthesis and characterization of polymorphic mixed-valent AuSe ($Au^{1+}Au^{3+}Se_2$) by varying the sequence of the addition of the precursors in a colloidal synthesis. Despite the variations, all produced materials showed the co-existence of α- and β-AuSe. Although both polymorphs were observed, XRD showed that the addition of the gold precursor at higher temperatures resulted in α-AuSe being the dominant phase while the addition at lower temperatures resulted in β-AuSe being preferred. The crystal structures of both α- and β-AuSe consist of repeating units of linearly bonded Au^{1+} ion to two Se atoms and Au^{3+} ion bonded to four Se atoms in a square planar geometry. The Au4f core level spectrum of the XPS, showed only the Au^{+1} oxidation state, however, using the Se3d core level spectrum, the formation of AuSe ($Au^{+1}Au^{+3}Se_2$) was evident. Using DFT calculations, the Raman spectra of α- and β-AuSe were simulated and only the square planar geometry was found to be Raman active. The square planar geometry $(Au^{3+}Se_4)^-$ ions belonging to the D_{4h} point group produced three Raman active vibrational modes, namely, a symmetric stretch (A_{1g}), a planar bending (B_{1g}) and an asymmetric stretch (B_{2g}) for α-AuSe as well as A_{1g} and B_{1g} for β-AuSe. Experimentally, all samples showed Raman vibrational lines from both phases. Moreover, Raman spectroscopy confirmed the presence of Au^{3+} in AuSe which was not detected using XPS. From the TEM and SEM results, it was evident that the morphologies of the predominantly α-AuSe samples were nanobelts while the predominantly β-AuSe samples showed plate-like structures. The predominantly α-AuSe samples showed a broad absorption band with a maximum at 853 nm while the predominantly β-AuSe samples showed evidence of absorption however with no defined excitonic peak.

Keywords: Gold selenide; structural properties; optical properties

1. Introduction

The discovery of graphene and its benefits in the early 2000s brought much interest to this two-dimensional material and opened new avenues into the investigations of similar materials and their potential in various applications. It revolutionized the way in which bulk layered materials were perceived, i.e. they could now exist as low-dimensional structures (zero-, one- & two-dimensional) with completely different physical, chemical, and optical properties. These layered materials consist of monolayers of covalently bonded atoms held together by relatively weak van der Waals forces [1]. Most emerging 2D materials are derived from structures that are layered in the bulk [2]. When determining material properties, dimensionality is a defining parameter because restrictions in one or more dimensions can alter the properties of the material. For example, the optical and electronic properties of the transition metal dichalcogenide MoS_2 change from indirect to direct bandgap when transitioning from a multilayer structure to a monolayer, a behaviour arising from d-orbital related interactions [3, 4]. Some qualities and properties of these 2D materials that have made them advantageous include (i) being atomically thin and providing a larger surface area due to the complete exposure of surface atoms, (ii) having the edge sites chemically more reactive than basal planes and the open van der Waals gaps enabling the intercalation and (iii) the mechanical strength and flexibility at atomic dimensions allowing them to be used in next-generation wearable electronics [5].

A reasonable amount of research has been conducted and reported on some layered transition metal chalcogenides such as MoS_2, InSe, In_2S_3, $CuSe_2$ [6-8] however, very little information is available on the noble metal chalcogenide gold selenide (AuSe), a layered material in the bulk. Due to its metallic conductivity, it can find use in applications similar to those of graphene such as being electrode materials in batteries, supercapacitors, and solar cells. The mixed valent inorganic compound $Au^+Au^{3+}Se_2$, simplified/reduced as AuSe, has a highly crystalline structure and belongs to the C2/m space group with two known phase modifications α- and β-AuSe [9, 10]. The two polymorphs can be easily distinguished by their most intense reflections along the (310) crystal plane for α-AuSe and the (111) crystal plane for β-AuSe. In a recent publication, Machogo *et al.* detailed the first colloidal synthesis of AuSe and noted the co-existence of both alpha and beta phase in the material regardless of the Au/Se mole ratios or time or temperature employed [11]. In addition to co-crystallization of both the alpha and beta form, elemental gold

and selenium have also been found to readily crystallize out as impurities. Finally, the last of the crystallization challenges is the conundrum of the oxidation state of gold in gold selenide. As previously mentioned, using crystallography, AuSe has been shown to be a mixed valence compound with gold present at oxidation state +1 and +3 [12]. However, a few studies using X-ray photoelectron spectroscopy have shown only the existence of Au^{1+} oxidation state, therefore making it difficult to corroborate the crystallography results [11]. Herein, in an added attempt to produce pure phase AuSe, the order of precursor addition was varied. Previously, Ntholeng *et al.* showed that the sequence of adding the precursor can result in the elimination of impurities as the result on the influence on the nucleation and growth process [13]. In addition, XPS and Raman (theoretical and experimental) spectroscopy studies were performed to further probe the structure of AuSe in order to establish the mixed valency of gold.

2. Experimental

2.1 Chemicals

Gold (III) chloride hydrate 99%, 99% elemental selenium powder, 70% oleylamine (OLA), toluene and 96% absolute ethanol were obtained from Sigma Aldrich and used without any further processing.

2.2 Synthesis of the different materials of gold selenide

A. In a three-neck round bottom flask, inert conditions were achieved by passing nitrogen gas 20 min before precursor addition and continued until the reaction was terminated. Under strong magnetic stirring and reflux, 15 mL of clear OLA was heated to 100 °C followed by the addition of 0.28 g selenium dissolved in 5 mL of OLA which turned the solution light grey, the temperature was further raised to 200 °C and at this point 0.17 g gold chloride dissolved in 5 mL of OLA was subsequently added turning the reaction mixture black. The reaction was carried out at 200 °C and aged for 1 hour.

B. Reaction B was a reverse to the one mentioned in A above; in a three-neck flask, under strong magnetic stirring, 15 mL of clear OLA was heated to 100 °C followed by the addition of gold chloride in 5 mL OLA upon which the solution turned orange, the temperature was raised to 200 °C and 5 mL Se-OLA was then added finally changing the

colour of the solution to black. The reaction was carried out at 200 °C under inert conditions and aged for 1 hour.

C. In a simultaneous addition reaction; 25 mL clear OLA was placed in a three-neck flask and heated to 200 °C under inert and strong magnetic stirring conditions. At this temperature both selenium powder and gold chloride crystals were added turning the mixture to black as a result of the immediate nucleation. The reaction was maintained at 200 °C, stirred and aged for 1 hour.

D. In a gradual heating reaction, oleylamine, selenium powder and gold chloride were all placed in a three-neck flask and the temperature was raised to 200 °C over a period of 20 min. The reaction mixture was initially light grey in colour but gradually turned black during the heating process. Once the temperature was reached the reaction was aged for 1 hour. The mixture was subjected to strong magnetic stirring and inert conditions during the heating as well as aging processes. The different addition sequences are summarised in Table 1.

After aging, the samples collected and allowed to cool naturally. Ethanol was added to flocculate the particles as well was to wash off any excess OLA. Following, the particles were collected by centrifugation at 7000 rpm and the black resultant powders were left to dry at room temperature.

Table 1: Table showing the sequence of precursor addition (where ▲ denotes heating)

Reaction A	OLA →	100 °C Add Se ▲	200 °C Add Au ▲
Reaction B	OLA →	100 °C Add Au ▲	200 °C Add Se ▲
Reaction C	OLA	→ ▲	200 °C Add Au & Se
Reaction D	OLA, Au & Se	→ ▲	200 °C

2.3 Characterization

X-ray diffraction

A Bruker D2 phaser (D2-205530) diffractometer using secondary graphite monochromated CuKα radiation (λ 1.5418 Å) at 30 kV and 10 mA was used to measure powder XRD patterns on the as-synthesized material. Measurements were taken using a glancing angle of incidence detector at an angle of 2˚, for 2θ values over 5 - 90˚ in steps of 0.036˚ with a step time of 0.5s and at a temperature of 294 K.

X-ray photoelectron spectroscopy

X-ray photoelectron spectroscopy (XPS) measurements were performed with a Physical Electronics PHI 5700 spectrometer with a multi-channel hemispherical electron analyzer. Non-monochromatic MgKα X-ray (300 W, 15 kV, 1253.6 eV) was used as excitation source. The spectrometer energy scale was calibrated using Cu 2p3/2, Ag 3d5/2, and Au 4f7/2 photoelectron lines at 932.7, 368.3, and 84.0 eV, respectively. Samples were mounted on a sample holder without adhesive tape and kept overnight at high vacuum in the preparation chamber before being transferred to the analysis chamber for testing. The spectra were collected in the constant pass energy mode at 29.35 eV. The residual pressure in the analysis chamber was maintained below 1.33×10^{-7} Pa during the spectra acquisition.

Raman spectroscopy

Raman analysis was performed using a T64000 series II triple spectrometer system from HORIBA scientific, Jobin Yvon Technology. The Raman spectra were obtained using 514.5 nm argon laser, through an Olympus microscope with a 50 X objective lens and laser power of 1.5 mW.

Computational calculations

The first-principles calculations based on density functional theory (DFT) [14] was executed using CASTEP module in Materials Studio developed by Accelrys Software Inc. The generalized gradient approximation with the scheme of Perdew–Bruke–Ernzerhof (GGA–PBE) [15] was utilized to represent the exchange-correlation functional in the DFT formalism. The α- and β-AuSe were generated using the crystal data reported by Rabenau *et al*. [12] as the initial

structure and was optimized using CASTEP. Norm conserving pseudopotential was employed to describe the electron–ion interactions and plane-wave basis sets were used to represent electronic wave functions. The custom energy cut-off of plane wave basis was set to 990 eV, and the convergence criterion of electronic self-consistency was set to 5.

Electron microscopy

Transmission electron microscopy (TEM) was carried out on a FEI Technai T12 TEM microscope operated at an acceleration voltage of 120 kV with a beam spot size of 2 in TEM mode and an EDX detector, operated at 120 kV. The samples were initially suspended in toluene this was followed by placing a drop of the suspended nanomaterials, on a lacey-carbon copper grid. The grid with the sample was then allowed to dry at room temperature before analysis. Scanning electron microscopy (SEM) was carried out on a FEI Nova Nanolab 600 FIB/SEM microscope. The powder samples were mounted on aluminium stubs with carbon tape and coated with one layer (5nm) chromium. High angle annular dark field (HAADF) scanning transmission electron microscope (STEM) images and energy dispersive X-ray (EDX) mapping images were acquired using a JEOL JEM 2100 instrument operated at 200 kV.

Ultra Violet-Visible spectroscopy

A Specord 50 AnalytikJena UV-Vis spectrophotometer was used to carry out the absorption measurements. The nanomaterials were dispersed in toluene and placed in a quartz cuvette of 1 cm path length for absorption analyses.

3. Results and discussion

Colloidal synthesis is a favourable approach in that it is convenient and reproducible for fabricating nanocrystals with controlled size and shape using simple inexpensive and less energy-demanding processes and equipment [16]. During synthesis, various parameters such as time, temperature, solvent and starting materials can be altered thereby producing nanomaterials of a desired nature. Herein, the sequence in which the precursors were added was altered, thus, obtaining the following results. The black powdered samples were characterized by X-ray diffraction and the diffractograms are shown in Figure 1. All four reactions showed the presence of both α-AuSe (JCPDS card 00-020-0457), and β-AuSe (JCPDS card 00-020-0458).

Nevertheless, it was evident that the addition of gold at 200 °C (reaction A and C) resulted in the α-phase being more predominant whilst the β-phase became more dominant when the gold source was added at lower temperatures (reaction B and D). The formation of particles in a colloidal synthesis is thought to be governed by the nucleation and growth process described by Lamer and Dinegar [17]. The formation of the nuclei is a critical step and determines the overall properties of the resultant particles. In reaction A and C, initially, selenium nuclei are formed and upon the addition of the gold precursor at 200 °C, α-AuSe is produced. The concentration of selenium ions thereafter drops and this favours the formation of β-AuSe as there is excess of gold ions. The excess gold nuclei then form gold nanoparticles hence the observed gold peaks (JCPDS card 00-004-0784) with relatively high intensities.

On the contrary, the addition of the gold precursor at low temperatures results in a gold-rich environment and favours the formation of β-AuSe as previously reported by Rabenau *et al.* [18]. However small traces of gold are still observed in reaction B; previously Machogo *et al.* showed that regardless of the Au:Se ratio, gold still persists [11]. In addition there's a large excess of selenium (JCPDS card 00-006-0362) observed for the reaction D. The heating up of both precursors from room temperature (reaction D) is evidently a less desirable route as it produces both Se and Au impurities at significant amounts.
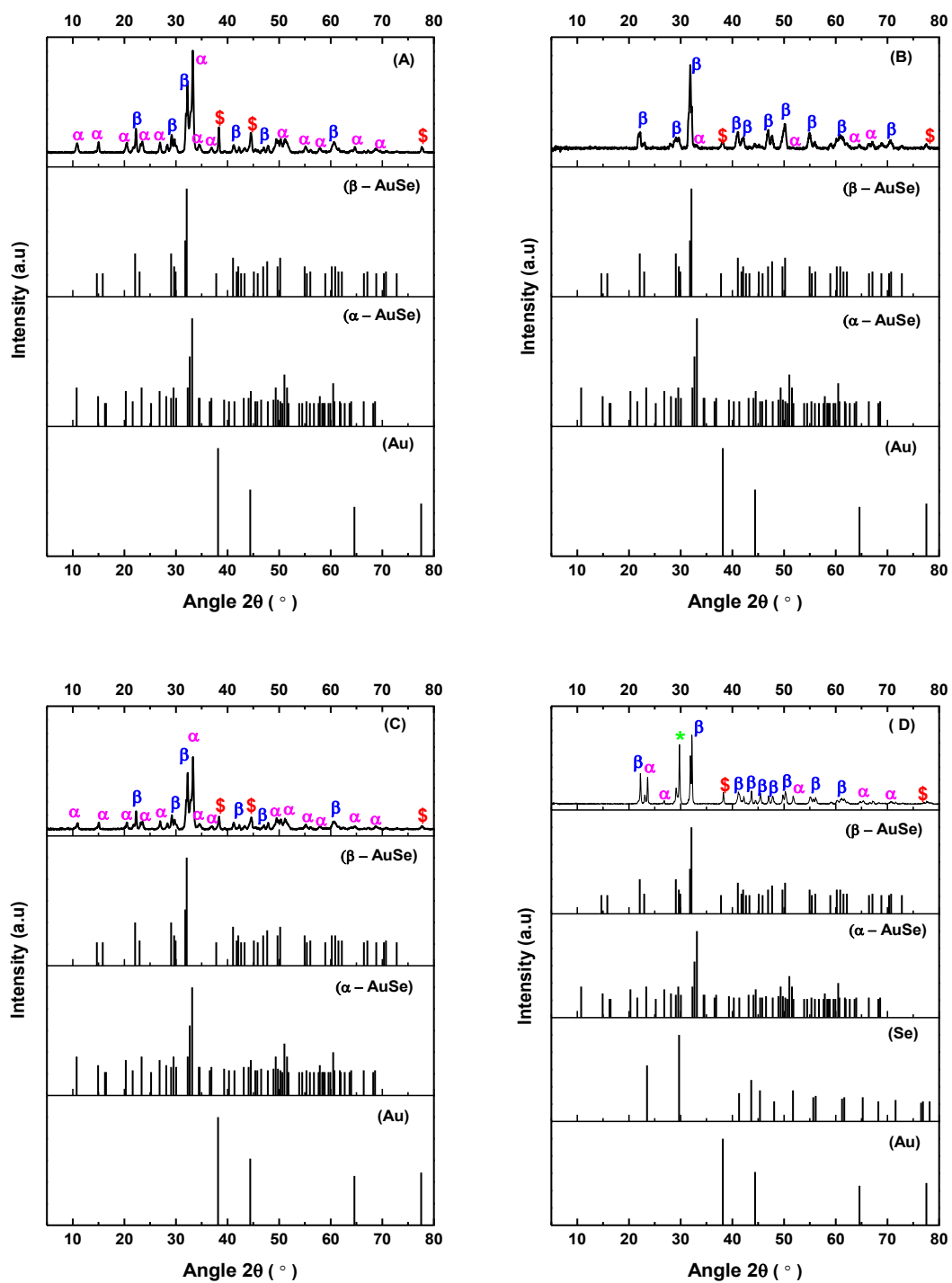
Figure 1: Standard XRD patterns of α-AuSe, β-AuSe, elemental Au and elemental Se together with XRD patterns of as-synthesised materials using the different reaction methods A - D.

(Key: α = α-AuSe, **β** = β-AuSe, **$** = elemental Au and ***** = elemental Se)

To further probe the structure of the nanomaterials, XPS was performed. The structure of gold selenide has presented some controversy as previously articulated by Machogo *et al.* and most recently by Vorobyev *et al.*; in particular, the presence of both Au^+ and Au^{3+} in the crystal structure [11, 19]. The crystal structures of the two α- and β-AuSe polymorphs consists of Au^{1+} ions coordinated linearly by two selenium atoms while Au^{3+} ions are bonded to four selenium atoms in square planar geometry as shown in Figure 2 [12]. Aside from the reported crystallographic data, there is no other confirmation of the existence of both oxidation states.
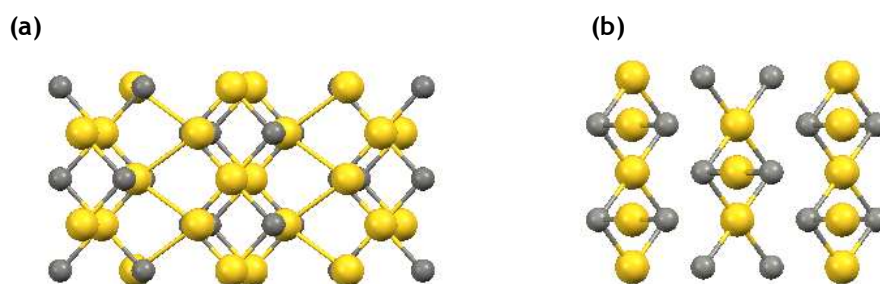
(a)   **(b)**

Figure 2: Crystal structure of (a) α-AuSe and (b) β-AuSe [12].

Shown in Figure 3 is the XPS survey spectrum of sample A. The spectrum shows a strong C1s peak confirming the presence of carbon due to the capping agent on the surface of the nanostructures. The attribution of the carbon peak to the capping agent is consistent with other reported work on capped nanoparticles and XPS has in fact been used to trace ligand exchange on the surface of the nanocrystals [20, 21]. The O1s peak is attributed to the oxidation of the capping agent due to the adsorption of oxygen from the atmosphere. Also observed were the selenium and gold peaks attributed to gold selenide.
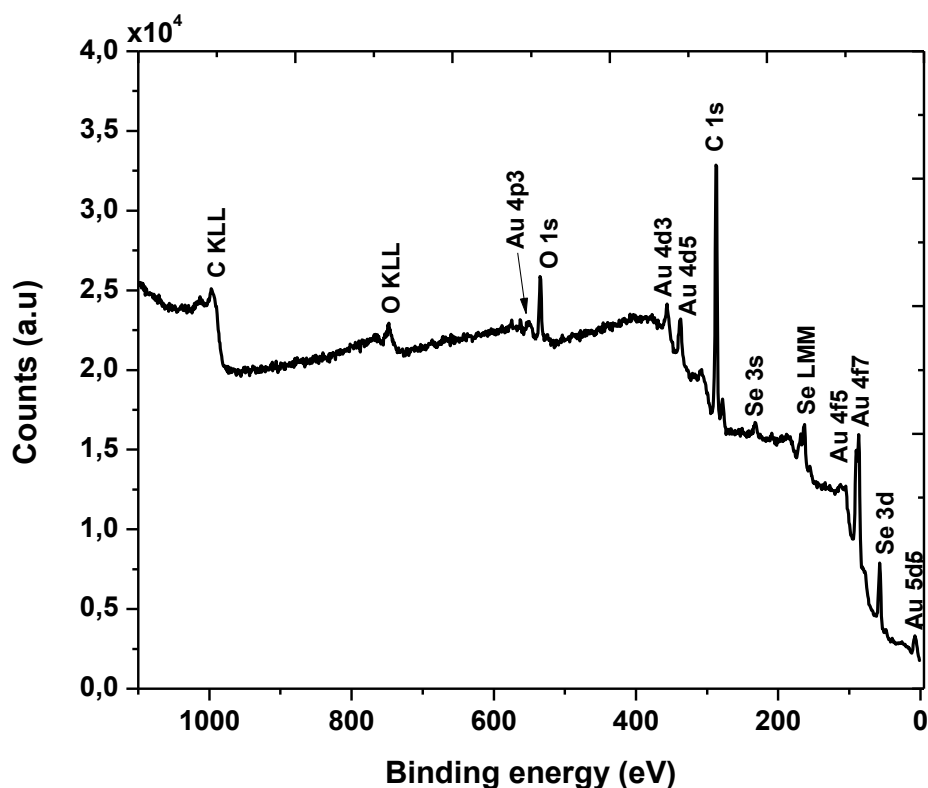
Figure 3: XPS survey spectrum of gold selenide sample produced from method A.

The high resolution XPS spectra with the focus on C1s, O1s, Au4f, and Se3d were done to evaluate the surface in more detail (Figure. 4). The C1s core level spectrum showed a single C-C peak attributed to the oleylamine. The O1s peak also showed a single peak ascribed to the oxidation of the capping agent. Shown in Table 2 is the atomic % composition and peak area %. The large amount of carbon, 79.5%, is of course expected and is attributed to the capping agent that forms a large organic shell around each particle. The relatively low amount of oxygen (8.9%) further suggests that the AuSe core is protected from oxidation by the thick capping agent shell. The Au4f core level spectrum is characterized by four components composed of the $4f_{7/2}$ peaks at 83.7 eV and 84.9 eV attributed to Au^0 and Au^{1+} respectively. In addition, $4f_{5/2}$ peaks were also observed for Au^0 and Au^{1+} oxidation states at 87.4 and 88.7 eV. The presence of Au^0 suggests the formation of gold nanoparticles. The presence of zerovalent gold was detected by XRD, however, the particles were not observed in the TEM. α-AuSe and β-AuSe as previously stated are mixed-valent compounds comprising of Au^{1+} and Au^{3+} ions, however, the XPS results

only shows the presence of Au^{1+} species. The complexities of probing both the +1 and +3 states of mixed-valent compounds have also been observed in AgO [22]. AgO has an identical crystal structure to AuSe where Ag^{1+} is coordinated linearly to two oxygens and Ag^{3+} is coordinated to four oxygens in a square planar geometry [23]. The XPS studies of AgO have been a subject of controversy where a number of explanations have been suggested as indicative of the presence of the Ag^{3+} peak. Observations of small peak shifts and large FWHM of the Ag^{1+} peaks as compared to the Ag^0 peaks have been attributed to the presence of the Ag^{3+} [24, 25]. These conclusions are however not quite accurate for AuSe as the Au^{3+} shows a distinct peak at ≈ 87 eV as previously reported in $HAuCl_4$ [26] and therefore does not overlap closely with the Au^{1+} peak as opposed to Ag^{1+} and Ag^{3+} peaks.
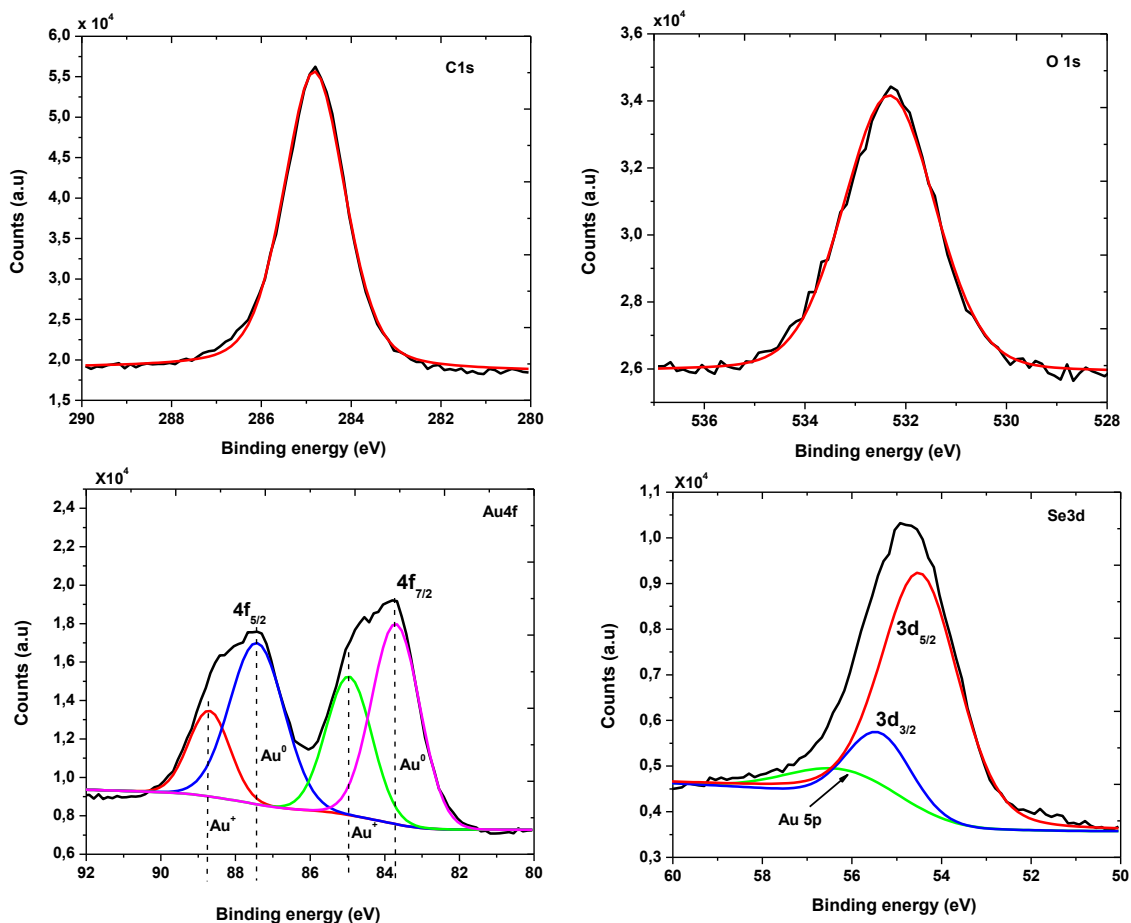

Figure 4: High resolution core level spectra of AuSe with focus on C1s, O1s, Au4f and Se3d.

To ascertain whether indeed gold is bonded to selenium, a Se3d core level spectrum is shown in Figure 4. The spectrum can be deconvoluted to three peaks attributed to the $3d_{5/2}$ (54.50 eV), $3d_{3/2}$ (55.42 eV) and Au5p (56.40 eV). The negative shift in the binding energies of the selenium peaks as compared to Se^0 can be attributed to the charge transfer from Au to the more electronegative selenium (Allred-Rochow electronegativity of Se is 2.48 versus 1.42 for Au) [27]. This, therefore, suggests the formation of AuSe. In addition, the presence of the Au5p peak, further suggests the bonding of the selenium to gold. Therefore, the Se core level spectrum strongly suggests the formation of AuSe and is thus in agreement with the observed XRD data.

Table 2: Summary of the atomic composition stoichiometric assignments obtained from the fitting of the XPS spectra reported in Figure 4

Element	Atomic %	Peak Binding energy (eV)	Assignments	Peak area %
C	79.5	284.8	C-C	100
O	8.9	532.3	C-O	100
Au	2.7	83.7	Au^0 $(4f_{7/2})$	34.1
		84.9	Au^{1+} $(4f_{7/2})$	22.3
		87.4	Au^0 $(4f_{5/2})$	31.1
		88.7	Au^{1+} $(4f_{5/2})$	12.4
Se	7.6	54.5	$3d_{5/2}$	73.9
		55.4	$3d_{3/2}$	16.2
		56.4	$Au5p_{3/2}$	9.9

Raman spectroscopy was used as an additional tool to further probe the structure of gold selenide. Calculations of the Raman spectra of both α-AuSe and β-AuSe were executed using crystal data emanating from the crystal structure in Figure 2 [12]. Using the data, only the square planar geometry showed Raman activity.
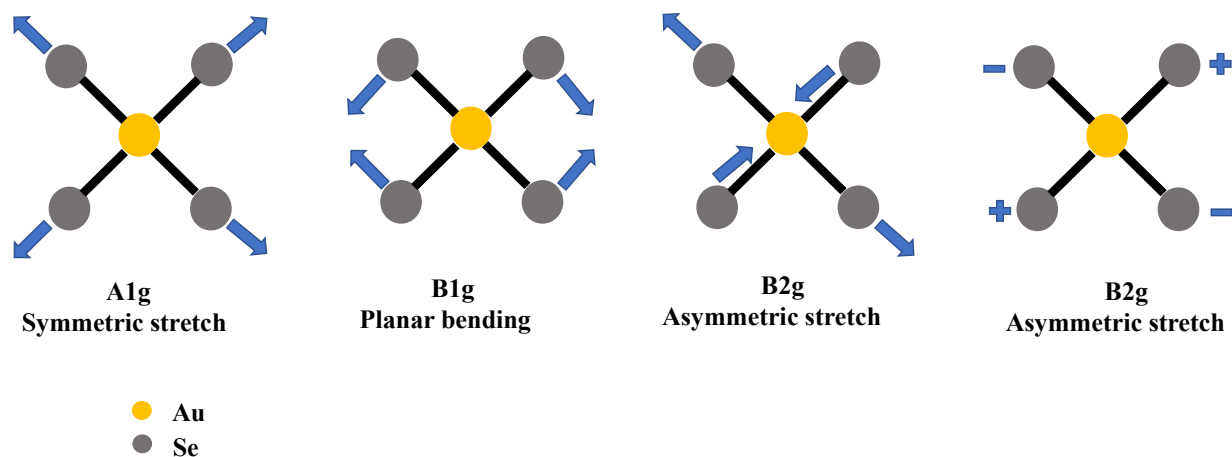
Figure 5: Schematic representation of D_{4h} point group Raman active vibrational modes of square planar $(Au^{3+}Se_4)^-$ molecule.

Square planar molecules of MX^{n-} nature such as $(ICl_4)^-$, $(PtCl_4)^{2-}$ and $(AuCl_4)^-$ belong to the D_{4h} point group and their similarity to the $(Au^{3+}Se_4)^-$ ions in the current study was used to explain the obtained data. According to molecular symmetry, molecules belonging to D_{4h} point group give rise to seven vibrational normal modes of which three are Raman active and Figure 5 gives a schematic representation of these Raman active normal modes. Figure 6(i) shows the theoretical Raman spectra of α-AuSe and β-AuSe together with the experimental data for samples A and C, while Figure 6(ii) shows the theoretical Raman spectra of α-AuSe and β-AuSe together with the experimental data for samples B and D. From the theoretical α-AuSe spectrum, three peaks are observed. The intense shift at 232 cm^{-1} is attributed to the A_{1g} normal mode and is due to the symmetric stretching of the Au–Se bond. The peak at 265 cm^{-1} is attributed to the antisymmetric stretching B_{2g} mode while the low intensity peak at 176 cm^{-1} is assigned to the B_{1g} normal mode for planar bending. The calculated Raman spectrum of β-AuSe showed two prominent vibrational peaks at 201 cm^{-1} and 306 cm^{-1} which were assigned to symmetric A_{1g} and antisymmetric stretching B_{2g}, respectively. These theoretical assignments were in agreement with reported experimental vibrational modes of square planar pentatomic complex halides [28]. With mixed valent AgO ($Ag^+Ag^{3+}O_2$) being an analogue to AuSe, i.e. Ag^+ is linearly bonded to two oxygen atoms while Ag^{3+} takes on a square planar geometry, it was of interest and therefore fitting to compare the Raman activity of AgO with that of AuSe. Three vibrational normal modes were observed similar to that of α-AuSe [29].
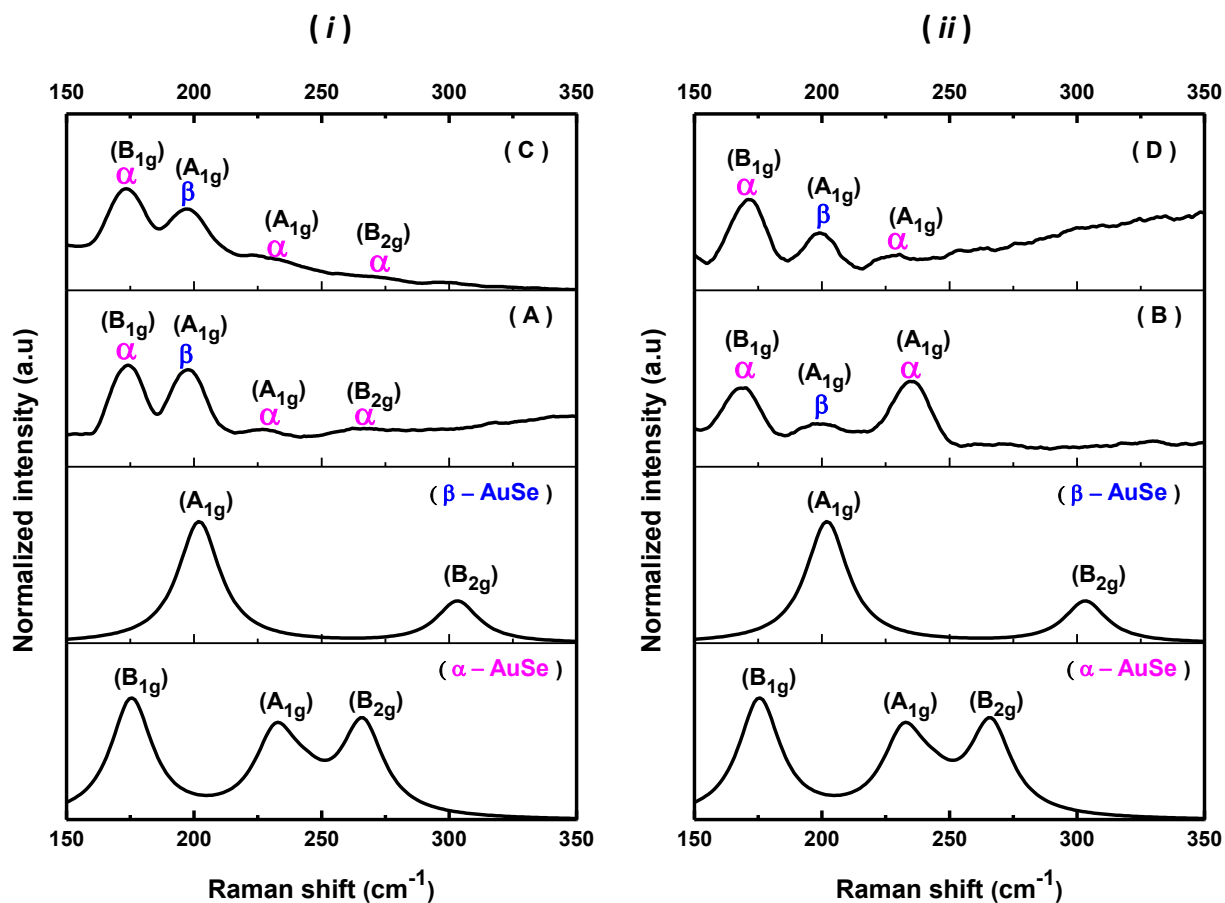
Figure 6: *(i)* Calculated Raman spectra of α-AuSe and β-AuSe and experimental Raman spectra of as-synthesized AuSe of sample A and C, *(ii)* calculated Raman spectra of α-AuSe and β-AuSe and experimental Raman spectra of as-synthesized AuSe of sample B and D.

The Raman spectra of the particles synthesized via methods A, B, C and D are also shown in Figure 6. The particles synthesized using methods A and C (Figure 6(*i*)) revealed a mixture of α- and β-AuSe. The bending vibrations (B_{1g}) in both samples (A and C) was observed at slightly lower wavenumbers at 173 cm^{-1} and 174 cm^{-1}, respectively compared to the theoretical Raman peak of α-AuSe where the peak was observed at 176 cm^{-1}. The α-AuSe symmetric and antisymmetric stretching vibrations of A and C were observed at 224 cm^{-1}, 226 cm^{-1} and 263 cm^{-1}, 269 cm^{-1}, respectively. In addition to the α-AuSe peaks, one peak assigned to β-AuSe symmetric stretching vibration at 196 cm^{-1} for both samples A and C was observed. The shifts in the Raman peaks can be as a result of a number of things such as (i) peaks shifts are observed when layered materials transition from bulk to 2D monolayers [30], (ii) through presence of

defects including extrinsic impurities [31] and (iii) lattice strain induced by defects or type of morphology [32]. The Raman spectra of samples B and D are shown in Figure 6(*ii*). Of evidence was the disappearance of the α-AuSe antisymmetric stretching vibration (B_{2g}) in both samples B and D. The bending mode (B_{1g}) of α-AuSe phase for sample B was observed at 168 cm^{-1} and that of sample D was observed 170 cm^{-1}, while the A_{1g} symmetric stretching vibration of the α-AuSe phase was observed at 235 cm^{-1} and 229 cm^{-1} respectively. A symmetric stretching vibration of β-AuSe phase was observed at 198 cm^{-1} and 199 cm^{-1} for B and D, respectively. These results revealed that all samples (A, B, C and D) contained both α- and β-AuSe phases, with sample A and C dominated by peaks of the α-phase. Bands not identified may be either very weak or obscured by highly intense bands. The frequencies of the Raman shifts are summarized in Table 3.

Table 3: Summary of the Raman frequencies and their vibrational assignments

Assignments	B_{1g} Planar bending (cm^{-1})	A_{1g} Symmetric stretching (cm^{-1})	B_{2g} Antisymmetric stretching (cm^{-1})
Theoretical α-AuSe	176	232	265
Reaction A	173	224	263
Reaction B	168	235	-
Reaction C	174	226	269
Reaction D	170	229	-
Theoretical β-AuSe		201	306
Reaction A	-	196	-
Reaction B	-	198	-
Reaction C	-	196	-
Reaction D	-	199	-

To get the morphological properties of the nanomaterials, electron microscopy was performed. Figure 7 shows TEM micrographs of the different nanocrystals. Reactions A and C produced lightly contrasted AuSe nanobelts of various lengths and widths. Deposited on these nanobelts

were tiny spherical particles, these are shown as an insert in Figure 7A. This was also observed in previous experiments [11] and it was confirmed that the nanobelts were α-AuSe while the spherical particles deposited on top of the nanobelts were of β-AuSe nature. These findings also hold for the present study as XRD and Raman spectroscopy confirmed the presence of both polymorphs in samples A and C. Reaction B and D showed densely contrasted AuSe nanoplates with those in sample B having a larger size than in D. The nanoplates in B were hexagonal in shape with defined facets while those in D had more cylindrical edges. Also observed on the Figure 7B and 7D, were trace amounts of nanobelts. The nanoplates were the predominant morphologies observed in reactions B and D and were therefore attributed to β-AuSe as confirmed by XRD as the dominant phase.
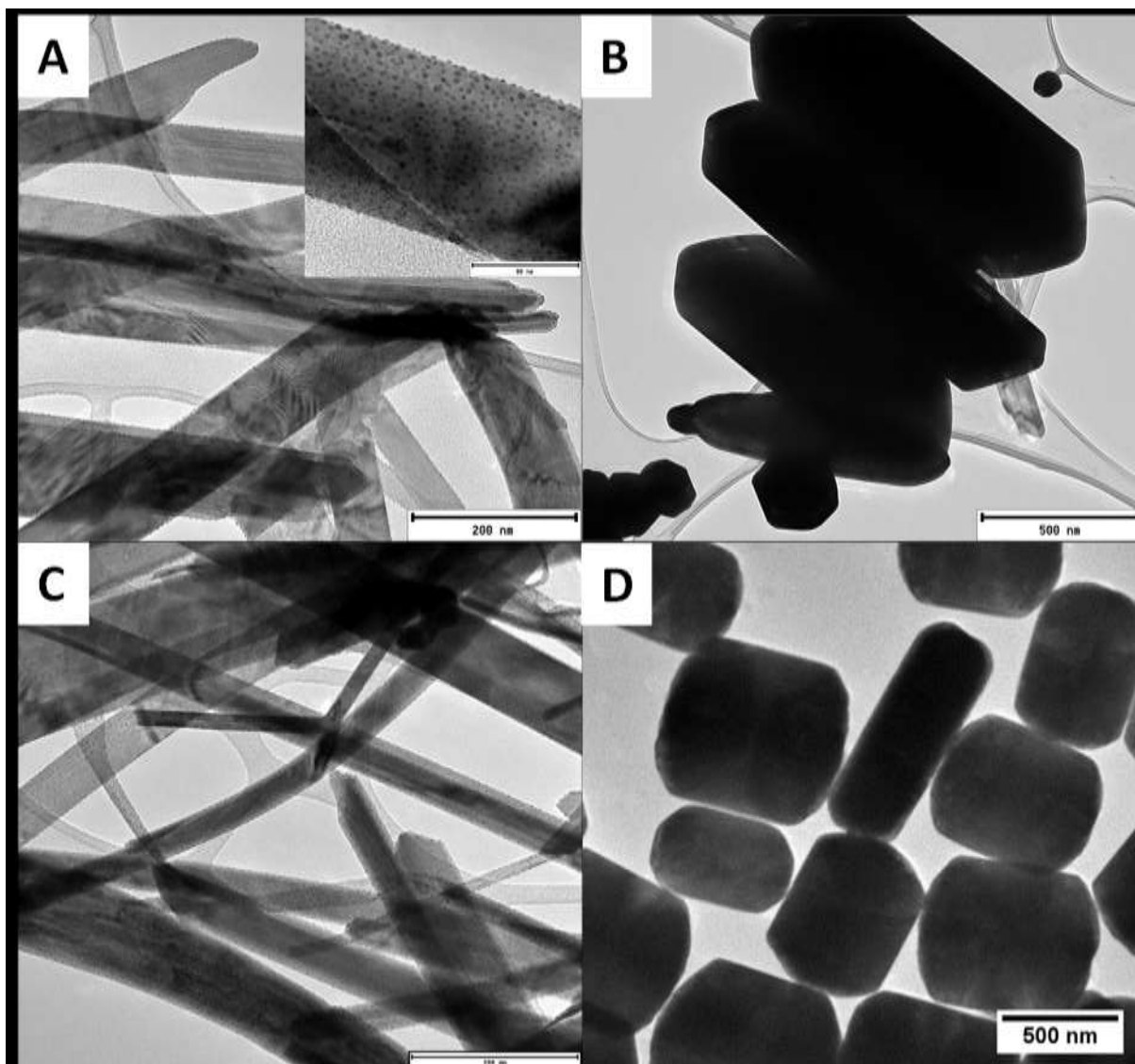
Figure 7: TEM images of as-synthesized AuSe nanocrystals using the different reaction methods A - D (insert highlighting the nanospheres deposited onto the belts).
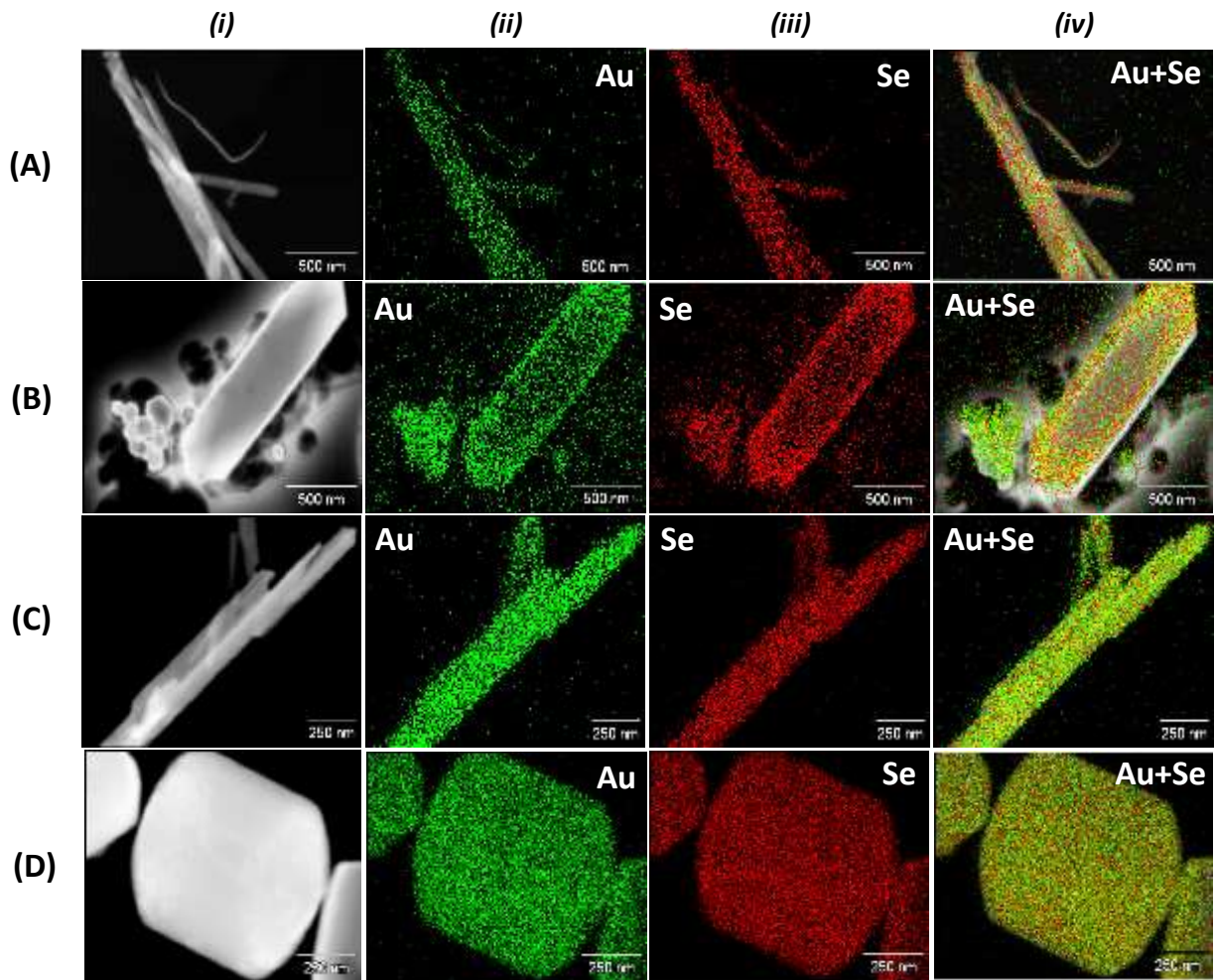
Figure 8: *(i)* HAADF STEM images of single nanocrystals from each sample A - D, *(ii)* elemental mapping of Au, *(iii)* elemental mapping of Se and *(iv)* summed elemental mapping of both Au and Se for samples A - D.

XRD and XPS confirmed the coordination of Au to Se and therefore the formation of AuSe, but in order to see the extent of homogeneity of the samples, TEM EDX mapping was performed and the results are shown in Figure 8. Column (i) shows the HAADF STEM images of the single nanostructures which were used as focus regions for each sample. Elemental mapping analysis in column (ii) depicts an even distribution of Au on the nanocrystals, equally, an even distribution of Se is observed in column (iii), for all samples. The summed mappings in column (iv) illustrates the uniformity in distribution of both elements giving complete homogenous AuSe nanomaterials.

Shown in Figure 9 are the SEM images of the synthesized materials. As previously observed in the TEM images, the nanobelts were obtained from reactions A and C whilst nanoplates were obtained in reactions B and D. For the nanoplates, the SEM images confirm that they are plates. The rod-like shapes appear to be plates lying on one side.
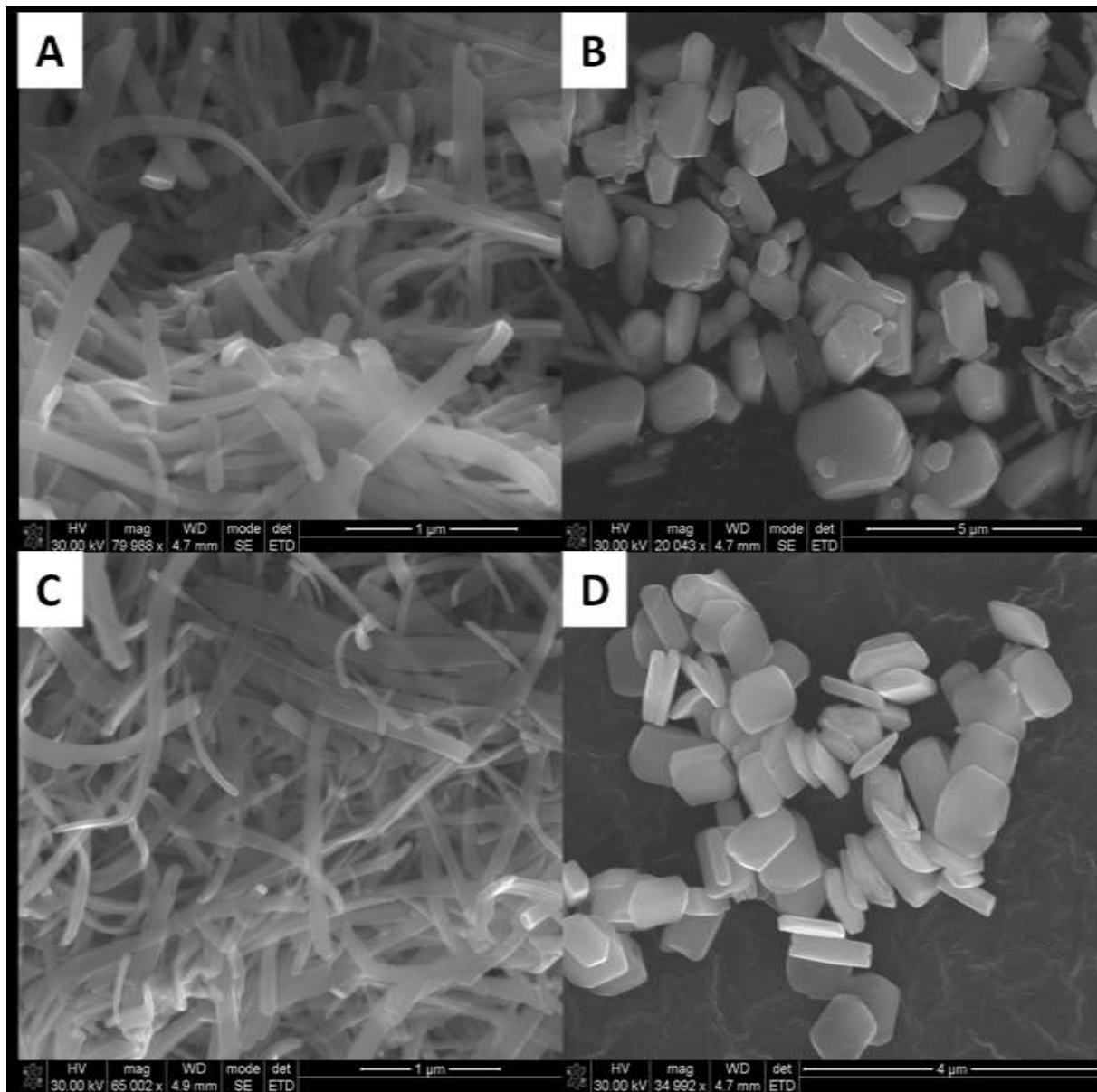

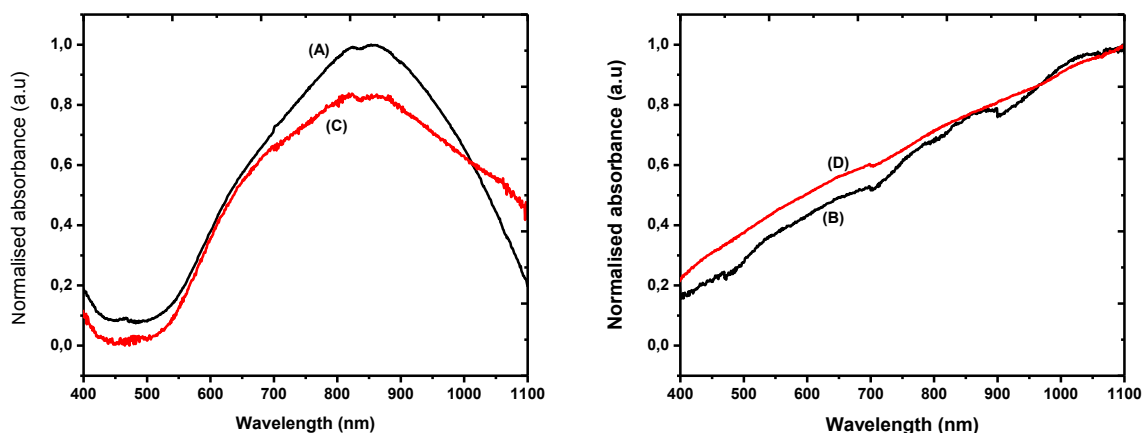**Figure 9:** SEM images of AuSe nanocrystals using the different reaction methods A - D.

Figure 10: UV-Vis absorption spectra of the as-synthesized AuSe.

To investigate the optical properties of the nanostructures, UV-Vis absorption spectroscopy was employed, and the obtained spectra are presented in Figure 10. The α-AuSe dominant samples from reaction A and C showed a large absorption band with a maximum at 853 nm. The broadness of the band is indicative of polydispersed samples. Metal chalcogenides with metallic conductivity such as $Cu_{2-x}Se$ (x > 0) and in this case AuSe have been shown to possess NIR localized surface plasmon resonance (LSPR) [33]. Samples from reactions B and D, the β-AuSe dominant samples illustrated an even larger absorption spectral window which spans from 400 nm well beyond 1100 nm (which is the spectral limit of the instrument). This together with the various shoulders observed, suggest that the samples are extremely polydispersed. This is consistent with the electron microscopy images presented above. The surface plasmon resonance (SPR) of gold nanoparticles is well known to be between approximately 500 nm - 600 nm depending on the size and shape [34]. XRD confirmed the presence of gold particle impurities for all samples, for sample A and C, a small shoulder peak slightly red-shifted from 600 nm can be attributed to large Au nanoparticles however it is impossible to assign any peaks for samples B and D.

4. Conclusion

In summary, colloidal synthesis was employed and produced polymorphic gold selenide nanomaterials. In all experiments, both α-AuSe and β-AuSe were formed, however, a level of dominance was observed depending on the sequence of precursor addition. XRD showed that α-

AuSe was the dominant phase when gold precursor was added at an elevated temperature contrary to the addition of gold at lower temperatures which presented β-AuSe as dominant. The Au4f core level spectrum in XPS was able to probe the Au^+ ions, additionally the Se3d core level spectrum showed evidence of the formation of AuSe with the presence of the Au5p peak suggesting bonding of the selenium to gold. Density Functional Theory calculations gave theoretical Raman spectra which were composed of 3 and 2 lines of Raman-active vibrational modes for α-AuSe and β-AuSe, respectively. Modes of both α- and β-AuSe were present in all four samples, further confirming the co-existence of both phases. Moreover, Raman confirmed the existence of Au^{3+} in the crystal structure further validating the mixed valency of the material. Electron microscopy highlighted the different shapes of these phases; α-AuSe being nanobelts while β-AuSe having plate-like morphology. Elemental mapping of the nanostructures illustrated an even distribution of gold and selenium across all samples confirming the homogenous nature of the nanomaterial. The broad absorbance bands in the UV-Vis spectra of both α-AuSe and β-AuSe showed LSPR in the NIR. These investigations accentuated the co-existence of both polymorphs of AuSe despite various attempts to isolate pure mono-phased AuSe nanomaterials. This could suggest some sort of co-dependence of one form on the other.

References

[1] M. Pumera, and A.H. Loo, Trends in Analytical Chemistry, 61 (2014) 49-53.

[2] A.J. Mannix, B. Kiraly, M.C. Hersam and N.P. Guisinger, Nature Reviews Chemistry, 1 (2) (2017) 0014.

[3] R. Mas-Balleste, C. Gomez-Navarro, J. Gomez-Herrero and F. Zamora, Nanoscale, 3 (1) (2011) 20-30.

[4] A. Splendiani, L. Sun,Y. Zhang, T. Li, J. Kim, C-H. Chim, G, Galli and F. Wang, Nano Letters, 10 (4) (2010) 1271-1275.

[5] K.S. Kumar, N. Choudhary, Y. Jung, and J. Thomas, ACS Energy Letters, 3 (2) (2018) 482-495.

[6] P.D. Matthews, P.D. McNaughter, D.J. Lewis and P. O'Brien, Chemical Science, 8 (6) (2017) 4177-4187.

[7] M.A. Airo, S. Gqoba, M.P. Kalenga, S. Govindraju, M.J. Moloto and N. Moloto, Journal of Crystal Growth, 406 (2014) 1-7.

[8] S. Gqoba, M. Airo, N. Ntholeng, L. Machogo, R. Sithole, M.J. Moloto, J. Van Wyk and N. Moloto, Materials Today: Proceedings, 2 (2015) 3901-3908.

[9] G.E. Cranton and R.D. Heyding, Canadian Journal of Chemistry, 46 (16) (1968) 2637-2640.

[10] J.E. Cretier and G.A. Wiegers, Materials Research Bulletin, 8 (12) (1973) 1427-1430.

[11] L.F.E. Machogo, P. Tetyana, R. Sithole, S.S. Gqoba, N. Phao, M.A. Ario, P.M. Shumbula, M.J. Moloto and N. Moloto, Applied Surface Science, 456 (2018) 973-979.

[12] A. Rabenau and H. Schulz, Journal of the Less Common Metals, 48 (1) (1976) 89-101.

[13] N. Ntholeng, B. Mojela, S. Gqoba, M. Airo, S. Govindraju, M.J. Moloto and N. Moloto, New Journal of Chemistry, 40 (12) (2016) 10259-10266.

[14] M.D. Segall, P.J.D. Lindan, M.J, Probert, C.J. Pickard, P.J, Hasnip, S.J. Clark and M.C. Payne, Journal of Physics: Condensed Matter, 14 (11) (2002) 2717-2744.

[15] J.P. Perdew, K. Burke and M. Ernzerhof, Physical Review Letters, 77 (18) (1996) 3865-3868.

[16] Y. Pu, F. Cai, D. Wang and J-F. Chen, Industrial & Engineering Chemistry Research, 57 (6) (2018) 1790-1802.

[17] V.K. LaMer and R.H. Dinegar, Journal of the American Chemical Society, 72 (11) (1950) 4847-4854.

[18] A. Rabenau, H. Rau, and G. Rosenstein, Journal of the Less Common Metals, 23 (3) (1971) 291-299.

[19] S. Vorobyev, M. Likhatski, A. Romanchenko, N. Maksimov, S. Zharkov, A. Krylov and Y. Mikhlin, Minerals, 8 (11) (2018) 492.

[20] A. Atewologun, W. Ge, A.D. Stiff-Roberts, Journal of Electronic Materials, 42 (5) (2013) 809-814.

[21] I-S. Liu, H-H. Lo, C-T. Chien, Y-Y. Lin, C-W. Chen, Y-F. Chan, W-F. Sue, S-C. Liou, J. Materials Chemistry 18 (6) (2008) 675-682.

[22] A.M. Ferraria, A.P. Carapeto, A.M. Botelho do Rego, Vacuum, 86 (12) (2012) 1988-1991.

[23] J.P. Allen, D.O. Scanlon and G.W. Watson, Physical Review B, 81 (16) (2010) 161103.

[24] J.F. Weaver, G.B. Hoflund, J. Physical Chemistry, 98 (34) (1994) 8519-8524.

[25] G.B. Hoflund, Z.F. Hazos, Physical Review B, 62 (2000) 11126.

[26] X. Zhang, H. Shi, B.-Q. Xu, Angewandte Chemie. Int. Ed. 44 (2005) 7132.

[27] A.L. Allred, E.G. Rochow, Journal of lnorganic and Nuclear Chemistry, 5 (4) (1958) 264-268.

[28] H. Stammreich and R. Forneris, Spectrochimica Acta, 16(3) (1960) 363-367.

[29] G.I.N. Waterhouse, G.A. Bowmaker and J.B. Metson, Physical Chemistry Chemical Physics, 3 (17) (2001) 3838-3845.

[30] H. Li, Q. Zhang, C.C.R. Yap, B.K. Tay, T.H.T. Edwin, A. Olivier and D. Baillargeat, Adv. Funct. Mater., 22 (2012) 1385-1390.

[31] S. Mignuzzi, A.J. Pollard, N. Bonini, B. Bennan, I.S. Gilmore, M.A. Pimenta, D. Richards and D. Roy, Phys. Rev. B, 91 (2015)195411.

[32] l. Yang, X. Cui, J. Zhang, K. Wang, N. Shen, S. Zeng, S.A. Dayeh, L. Feng and B. Xiang, Scientific Reports, 4 (2014) 5649.

[33] I. Kriegel, C. Jiang, J. Rodríguez-Fernández. R.D. Schaller, D.V. Talapin, Enrico da Como and J. Feldmann, J. Am, Chem. Soc., 134 (2012) 1583-1590.

[34] S.K. Ghosh and T. Pal, Chemical Reviews, 107 (11) (2007) 4797-4862.